



# Water Resources Research®

## RESEARCH ARTICLE

10.1029/2024WR038287

### Special Collection:

Drones for sensing freshwater ecosystems

### Key Points:

- We compared co-located, contemporaneous surface velocity measurements of tidal flow made by a drone and an in-channel acoustic profiler
- Surface velocity differences between the data sets can be partially explained by surface wind stress direction biasing remote measurements
- Trackable temperature patterns in drone-based thermal infrared images enabled surface velocimetry without additional passive tracer seeding

### Supporting Information:

Supporting Information may be found in the online version of this article.

### Correspondence to:

E. T. Heberlein,  
eth47@cornell.edu

### Citation:

Heberlein, E. T., Mayes, M., Morgan, B. E., Caylor, K. K., Schweitzer, S. A., & Cowen, E. A. (2025). Wind stress effects on drone-based thermal infrared surface velocimetry measurements of tidal flow in an estuary. *Water Resources Research*, 61, e2024WR038287. <https://doi.org/10.1029/2024WR038287>

Received 30 JUN 2024

Accepted 19 AUG 2025

Corrected 14 OCT 2025

This article was corrected on 14 OCT 2025. See the end of the full text for details.

### Author Contributions:

**Conceptualization:** Evan T. Heberlein, Edwin A. Cowen

**Data curation:** Evan T. Heberlein, Marc Mayes, Bryn E. Morgan

**Formal analysis:** Evan T. Heberlein

**Funding acquisition:** Evan T. Heberlein, Kelly K. Caylor, Edwin A. Cowen

© 2025. The Author(s).

This is an open access article under the terms of the [Creative Commons](#)

[Attribution License](#), which permits use, distribution and reproduction in any medium, provided the original work is properly cited.

## Wind Stress Effects on Drone-Based Thermal Infrared Surface Velocimetry Measurements of Tidal Flow in an Estuary

Evan T. Heberlein<sup>1</sup> , Marc Mayes<sup>2,3,4</sup> , Bryn E. Morgan<sup>2,5,6</sup> , Kelly K. Caylor<sup>2,5,7</sup> , Seth A. Schweitzer<sup>1</sup> , and Edwin A. Cowen<sup>1</sup> 

<sup>1</sup>DeFrees Hydraulics Laboratory, School of Civil & Environmental Engineering, Cornell University, Ithaca, NY, USA,

<sup>2</sup>Earth Research Institute, University of California, Santa Barbara, Santa Barbara, CA, USA, <sup>3</sup>Department of Watershed Sciences, Quinney College of Natural Resources, Utah State University, Logan, UT, USA, <sup>4</sup>Spatial Informatics Group-Natural Assets Laboratory (SIG-NAL), Pleasanton, CA, USA, <sup>5</sup>Department of Geography, University of California, Santa Barbara, Santa Barbara, CA, USA, <sup>6</sup>Now at Department of Civil and Environmental Engineering, Massachusetts Institute of Technology, Cambridge, MA, USA, <sup>7</sup>Bren School of Environmental Science and Management, University of California, Santa Barbara, Santa Barbara, CA, USA

**Abstract** We evaluate the effect of surface wind stress on remote velocimetry measurements of tidal flow by comparing these measurements to the bulk flow velocity measured by a co-located acoustic velocity profiler in a tidal channel. The remote velocity measurements are made with a thermal imager mounted on a drone hovering directly over the acoustic measurement location. Drones are a useful platform to support a variety of cameras and sensors for capturing images that can be used to infer surface velocities. Drone-mounted thermal infrared microbolometer cameras are a lower-cost infrared imaging solution that can detect subtle temperature patterns which naturally occur at the surface of many flows. These thermal patterns are used as signals for pattern-tracking to produce velocity measurements across the observed water surface. Drone flights were conducted at Carpinteria Salt Marsh Reserve (California, USA). Wind speed and direction relative to the flow direction caused the drone-based surface velocimetry measurements to deviate from in-channel surface-extrapolated acoustic velocity measurements. Drone-based velocity measurements were slower than in-channel velocity measurements when the parallel wind stress direction was opposite the tidal flow, while drone-based velocity measurements were faster than in-channel velocity measurements when the parallel wind stress and tidal flow were in the same direction. The effect of wind stress on remote surface velocimetry measurements is relatively unstudied, and herein we quantify this effect by comparing image-derived estimates to in-channel velocity measurements. This experiment also demonstrates the feasibility of drone-based thermal surface velocimetry measurements in an estuary.

**Plain Language Summary** This study explores how wind affects surface water velocity using an infrared camera on a drone in a salt marsh. Drones equipped with infrared cameras can capture temperature patterns on the water surface, the motion of which can be tracked to estimate water flow speeds. Drone-based remote sensing of surface water velocity offers expanded spatial coverage and keeps field researchers out of harm's way. However, wind's influence on the results of these measurements relative to the bulk flow has not been well studied. We compared drone-based velocity estimates to in-channel velocity measurements from an acoustic velocity profiler instrument at Carpinteria Salt Marsh Reserve in California. The drone measurements captured strong impacts of the wind stress on the surface velocity measurements, consistent with the physics. When the wind direction was opposite the tidal flow, the drone-based surface measurements were slower than the in-channel measurements. However, when wind and tidal flow moved in the same direction, the surface measurements were faster than the in-channel speed. This study shows that drone-based infrared imaging can be a useful tool for measuring water surface velocities in tidal environments like salt marsh estuaries, but also highlights potential challenges from wind.

### 1. Introduction

Remote measurements of water velocities are a powerful tool for observing surface and bulk characteristics of environmental flows. Drones, also known as unmanned aerial vehicles (UAV) or small uncrewed aircraft systems (sUAS), are a flexible and easily deployable platform for a variety of airborne imaging sensors capable of making

**Investigation:** Evan T. Heberlein, Marc Mayes  
**Methodology:** Evan T. Heberlein, Seth A. Schweitzer, Edwin A. Cowen  
**Project administration:** Evan T. Heberlein, Edwin A. Cowen  
**Resources:** Marc Mayes, Kelly K. Caylor, Edwin A. Cowen  
**Software:** Evan T. Heberlein, Bryn E. Morgan  
**Supervision:** Kelly K. Caylor, Seth A. Schweitzer, Edwin A. Cowen  
**Validation:** Marc Mayes, Bryn E. Morgan, Edwin A. Cowen  
**Visualization:** Evan T. Heberlein, Marc Mayes  
**Writing – original draft:** Evan T. Heberlein  
**Writing – review & editing:** Marc Mayes, Bryn E. Morgan, Kelly K. Caylor, Seth A. Schweitzer, Edwin A. Cowen

water velocity measurements (Eltner et al., 2020; Perks et al., 2016). Drone-mounted cameras capture nadir images with minimal perspective distortion, enabling synoptic and spatially explicit velocity measurements over areas of flowing surface waters such as rivers and estuaries. However, additional work is needed to test the effect of environmental factors like wind on the measurement results of this field velocimetry methodology relative to more conventional water velocity measurement instruments, such as acoustic Doppler current profilers (ADCPs). This experiment was therefore designed to compare drone-mounted surface velocimetry measurements relative to in-channel acoustic velocity profiler measurements of a tidally forced and wind-affected flow.

### 1.1. Image-Based Velocimetry Techniques

The pattern tracking techniques used here to remotely measure surface water velocities from aerial time series imagery are rooted in particle image velocimetry (PIV). PIV is a well-developed laboratory technique to quantify water velocities in digital images by tracking illuminated particles, producing time-varying velocity vectors of small spatially averaged regions across the entire field of view (FOV) (e.g., Cowen & Monismith, 1997). Large-scale PIV (LSPIV) is a primarily field-based application of PIV tracking algorithms to derive two-dimensional distributed surface velocities from oblique images, which are orthorectified to physical units (e.g., Eder et al., 2023; Muste et al., 2014). These remote velocity measurement techniques do not require the introduction of instruments such as acoustic velocity profilers into the water body, which avoids disturbing the flow being measured and keeps researchers out of harm's way under unsafe conditions, such as floods.

Large-scale PIV often requires the presence or introduction of trackable surface features, such as wood particles (Biggs et al., 2022; Kim et al., 2008), ice (Ettema et al., 1997), foam (Al-mamari et al., 2019), or suspended sediment (Legleiter & Kinzel, 2020) to produce accurate surface velocity measurements, and this requirement has given rise to two alternative field-based pattern tracking techniques, which are combined in this study. Space-time image velocimetry (STIV) consists of a one-dimensional pattern tracking technique where intensities along lines of pixels parallel to the flow direction are assembled into a space-time diagram with axis units of distance (along the pixel line) and time (from one image timestep to the next). The slope of pixel intensity patterns visible in the space-time diagrams represents the average velocity along one particular path in the image. This technique can be useful if insufficient surface features exist for two-dimensional large-scale PIV algorithms to be accurate (Fujita et al., 2019), especially with visible light imagery where surface features might not be evenly distributed. However, some detectable surface texture is required to derive accurate measurements from any velocimetry method using visible light imagery, including STIV. This requirement highlights a significant advantage of using thermal images for surface velocimetry. Infrared quantitative image velocimetry (IR-QIV—Schweitzer & Cowen, 2021) uses a thermal infrared camera with sufficiently precise thermal resolution (<0.1°C) to detect naturally occurring temperature variations on the surface of flowing water, providing a trackable signal across the water surface and removing the need to artificially seed the flow. These subtle temperature variations on the water surface or “skin” are a signature of surface processes such as atmospheric heat exchange and wave breaking, as well as bottom-generated turbulence in relatively shallow water bodies like estuaries (Brumer et al., 2016). Thermal infrared cameras are well-suited to detect these temperature variations due to the low penetration of thermal infrared radiation in water, on the order of  $10^{-5}$  m in depth (Zappa et al., 2003). Infrared imagery is particularly useful when flows of interest, such as snowmelt-driven floods (Fujita, 2017) or high tides, occur overnight, because sunlight is not necessary for infrared sensors to accurately detect the surface water temperature. Thermal infrared image quality is highest and thermal surface velocimetry methods are therefore most accurate when the air temperature is lower than the water temperature (Legleiter, Kinzel, Dille, et al., 2024), but it is typically not permissible to fly a drone at night when these conditions often occur.

This study builds on a variety of past work using thermal infrared imagery to measure tidal flows and wave dynamics in estuaries and the coastal ocean, where the undulating free surface is affected by tides, currents, and wind waves which have historically posed measurement challenges (Chickadel et al., 2009; Dugan et al., 2014; Laxague & Zappa, 2020; Schwendeman & Thomson, 2015; Sutherland & Melville, 2015). In open channels, surface velocity measurements have also been used to infer characteristics of bulk velocity and channel discharge throughout the water column (Levesque & Oberg, 2012), leveraging the physical relationship between surface turbulence and boundary-layer turbulence induced by bed shear over variable bathymetry (Johnson & Cowen, 2016).

The utility of drones as surface velocimetry tools has grown rapidly in the last decade. Consumer-grade visible light cameras mounted on a drone have been used to measure water surface velocity using seeded paper pellets and naturally occurring algae (Tauro et al., 2015), and quantify two-dimensional surface hydrodynamics using introduced dye tracers in branching salt marsh channels (Pinton et al., 2020). Uncooled thermal infrared microbolometer cameras have been incorporated into drone systems to conduct large-scale PIV on open channel flow in rivers (Eltner et al., 2021; Kinzel & Legleiter, 2019), detect groundwater discharge to the coastal ocean (Lee et al., 2016), and track infrared-emitting seed particles (Thumser et al., 2017). Hot water can also be introduced into environmental flows as a thermal tracer that is detectable with a microbolometer camera (Lin et al., 2019), although introducing additional water at a different temperature could theoretically change the characteristics of the flow being measured. Cooled thermal infrared cameras are now becoming light and power-efficient enough to be flown on multirotor drones for velocimetry applications measuring open-channel flow (Kinzel et al., 2024; Legleiter, Kinzel, Dille, et al., 2024), yielding images with better thermal resolution and less noise than uncooled microbolometer cameras.

All image velocimetry methods extract physical velocity measurements from images via a calibration process relating the locations of features in the images to real-world physical coordinates of those features. In field-based image velocimetry applications like large-scale PIV, this process often involves georeferencing features visible in the camera field of view using GPS, which also locates velocity measurements within a coordinate system on the earth's surface. A common technique involves the use of ground control points (GCPs), which are targets designed to be visible to the camera. By surveying GCPs using GPS, the relationship between the physical and image coordinates of these GCPs can be inferred and used to account for the camera's orientation and perspective distortion, providing physical coordinates for each pixel in the image (Holland et al., 1997). GCP-based georeferencing methods can be used to infer two-dimensional physical length scales in images as in this study, or three-dimensional relationships between objects in the field of view can be derived and used to process oblique imagery. General recommendations for drone-based velocimetry from Detert (2021) dictate that at least four GCPs are evenly distributed along the channel banks with some GCPs located near the corners of the drone-based imager's field of view, where radial distortion causes the highest spatial uncertainty in a georeferenced image from a nadir viewing angle (Schweitzer & Cowen, 2022). An alternative to GCP-based georeferencing of images collected from a stationary camera is structure from motion (Tomasi & Kanade, 1992), which can derive 3D spatial scales for a landscape or structure from a time series of 2D images taken from a moving camera on a drone. With regard to images of moving water collected from a stationary drone, ready-to-use image stabilization toolboxes have been developed as a pre-processing step for velocimetry (e.g., Pizarro et al., 2022).

The growing use of drones for surface velocimetry has coincided with increasing access to software tools for implementing this approach (e.g., Legleiter & Kinzel, 2023), highlighting the need to understand wind's effect on the output from these tools. Of the surface velocimetry research efforts that have addressed potential impacts of wind stress, these have primarily focused on the impact of wind on the presence of trackable surface texture and thresholds for valid results (Ansari et al., 2023; Brumer et al., 2016; Fairley et al., 2024; Lewis et al., 2018; Muste et al., 2005), or flight safety and stability of drone imagery (Koutalakis & Zaimes, 2022; Pearce et al., 2020), rather than the deviation of remote surface velocity field measurements from co-located, contemporaneous in situ near-surface measurements due to wind stress. Additionally, attempts to conduct thermal surface velocimetry of tidal flow from a drone in an estuarine setting have not been documented in the literature.

## 1.2. Objectives

Our study investigates wind stress effects on remote surface water velocity measurements, which reflect both the channel's bulk flow velocity and the wind-driven surface boundary layer. Measuring potential differences between average in-channel velocity and surface velocity will help identify conditions when surface-based inferences of bulk flow parameters might require particular care or caution. A small estuary presents an ideal setting for this experiment due to relatively consistent sea breeze winds and predictable tides, enabling observations of tidal flow both with and against the wind direction. Tidal flow velocity measurements were collected with a thermal infrared camera mounted on a drone. Drone flights were conducted immediately adjacent to a scientific-grade meteorological station, which presented an opportunity to assess the impact of wind stress on remote surface velocity measurements relative to contemporaneous and co-located in-channel velocity measurements from an acoustic velocity profiler. This study also presents a novel demonstration of this velocimetry method



**Figure 1.** Aerial overview of Carpinteria Salt Marsh Reserve and weather station location.

applied to a tidal flow, as we are not aware of previously published remote thermal surface velocities collected from an aerial drone in an estuary.

## 2. Materials and Methods

### 2.1. Study Site

The study was conducted at Carpinteria Salt Marsh Reserve (CSMR), a 93 ha protected tidal wetland in Santa Barbara County, California, USA, owned and managed by the University of California Natural Reserve System (Figure 1). The marsh receives seasonal runoff from Franklin and Santa Monica Creeks, and daily tidal exchange through a roughly 30 m wide inlet from the Santa Barbara Channel. While discharge is not continuously monitored on the creeks entering the salt marsh, the neighboring larger watershed immediately to the southeast (Carpinteria Creek) has a USGS gauging station that showed zero discharge during this study (USGS, 2022). Therefore, all flow measured during this experiment was assumed to be tidally driven. This experiment consisted of five repeated drone flights conducted during a 24-hr period starting at 12:00 Pacific time on 23 May 2022.

Many California estuaries open and close seasonally due to sediment transport and hydrological regimes: regional beaches are exposed to high wave energy and stream discharge in coastal watersheds has high seasonal variance (Clark & O'Connor, 2019). Despite its protection as a research reserve, channel modifications are occasionally implemented in CSMR for management purposes. CSMR underwent a dramatic ecological disturbance following the Thomas Fire in December 2017, when destructive debris flows deposited sediment over large areas of the marsh, resulting in a 222% increase in bare soil immediately following the debris flows and potential longer-term impacts to marsh type and plant diversity (Silva et al., 2022). Emergency dredging of marsh channels to prevent the adjacent town of Carpinteria from flooding was undertaken in CSMR after the January 2018 debris flows and again in spring 2023, after high winter rainfall increased mountain erosion and led to the deposition of large amounts of sediment in the marsh, which blocked tidal creek channels.

Demonstrating the potential of drone-based surface velocimetry in a salt marsh estuary is an important secondary outcome of this study, as this method could address some of the surface hydrology measurement challenges in these ecosystems. The geomorphology and ecological function of salt marshes is largely determined by

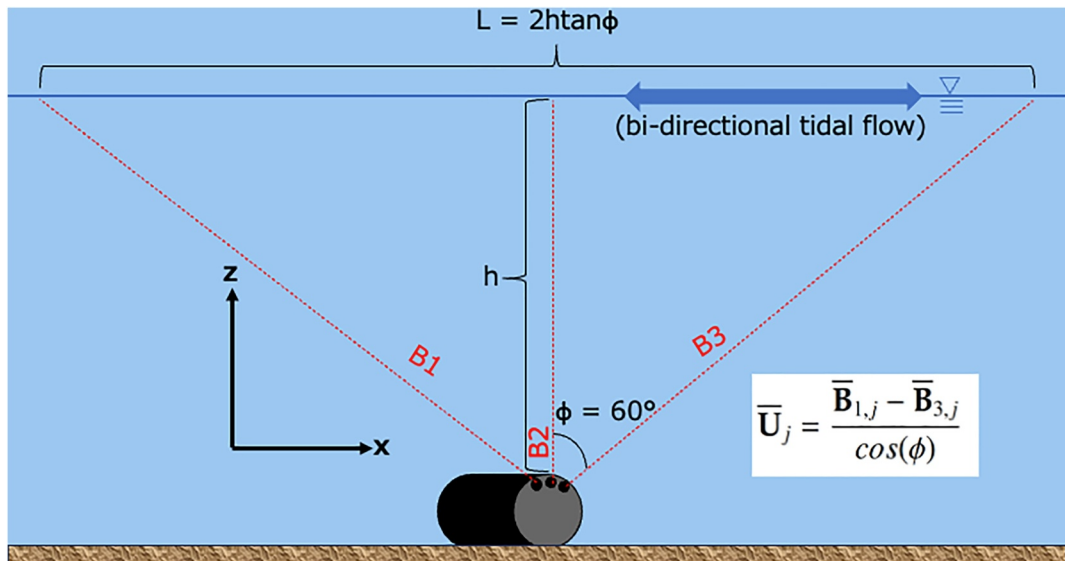


**Figure 2.** Beam orientations relative to coordinate system in the  $x - z$  plane of the Nortek AquaDopp acoustic velocity profiler. Note  $x$  is positive in the downstream, outgoing tide direction, and  $h$  denotes water depth. Inset formula shows calculation of streamwise velocity  $\bar{U}$  from the oblique beam velocities in the  $j$ -th vertical bin.

hydrodynamic conditions and sediment supply, and these physical characteristics are significantly impacted by submerged vegetation and even marsh herbivore population dynamics (Elmer, 2014; Friedrichs & Perry, 2001; Neumeier & Amos, 2006). Due in part to these dynamic biophysical interactions, salt marshes often exhibit complex branching hydrology, resulting in a wide range of hydrodynamic conditions and stage-dependent tidal transport pathways (Fagherazzi et al., 2008), which can limit the utility of point velocity measurements. Short-term salt marsh hydrodynamics are primarily driven by tidal elevation and resulting pressure gradients between two-directional tidal flow and freshwater inputs (Young et al., 2016), which over time influence marsh elevation through erosion and deposition of sediment (Voulgaris & Meyers, 2004). In light of the complex spatial and temporal dynamics of salt marsh hydrology and associated ecological processes, an easily deployable and mobile remote sensing system that can measure surface velocity presents a powerful tool for characterizing short-term hydrodynamic conditions across many channels in a given marsh.

## 2.2. Acoustic Profiler In Situ Velocity Measurements

The experiment consisted of repeated stationary drone flights over the same stretch of tidal channel where a Nortek AquaDopp profiler was deployed on the channel bottom, collecting “water-truth” velocity measurements to compare with the remotely sensed surface velocities measured from the drone. The AquaDopp continuously recorded streamwise (along-channel)  $u$ -velocities (in the  $x$ -direction) at 1 Hz in vertical bins of  $\Delta z = 1.5$  cm. The instrument was fitted with a head consisting of three beams aligned in the same plane in the along-channel direction, with beams 1 and 3 diverging from the vertical (beam 2) by  $60^\circ$  in opposite streamwise ( $x$ ) directions as seen in Figure 2.

The vertical profile of the  $x$  and  $z$  directed components of the velocity vector ( $u$  and  $w$ , respectively) is measured by assuming horizontal homogeneity (i.e., streamwise homogeneity) and using the beam geometry to calculate the two components of the velocity field in each range-gated bin elevation. The bin height was set at 15 mm and the data recorded in beam coordinates for post-processing. The water depth  $h$  in the tidal channel, which fluctuated with the tidal stage, was identifiable via a high amplitude response in  $B_2$ , since the free surface strongly reflects the acoustic signal from the AquaDopp back toward the instrument. Therefore, the free surface at each timestep was defined as the highest amplitude response bin in the vertical beam ( $B_2$ ). Using the geometry of the AquaDopp head, the corresponding surface bin in the oblique beams ( $B_1$  and  $B_3$ ) and the physical distance between the beams at the water surface was identified. The AquaDopp data were processed in 12-min intervals, coinciding with each flight hover time  $\pm$  a one-minute buffer.

**Table 1***Micasense Altum Infrared Microbolometer Band Specifications*

Resolution	160 × 120 pixels
Field of view	57° × 44.3°
Thermal sensitivity	<50 mK
Thermal accuracy	±5 K
Wavelength range	8–14 μm

AquaDopp data collected on May 23 before and during high tide, as shown in Figure 6, exhibited phase-wrapping in beam coordinates, meaning  $B_1$  and  $B_3$  would suddenly change sign for brief periods. Phase-wrapping is a somewhat common issue with acoustic velocity profilers, for example, if the beam pulse timing interval is too short, and beam data were phase-unwrapped by manually correcting these sign changes in beam coordinates. Phase-unwrapped beam data were then processed with an Adaptive Gaussian Window (AGW) filter (Cowen, 2006; Cowen & Monismith, 1997), which retained at least 95% of data in both oblique beams across all flights. Then  $u$  and  $w$  velocities were calculated from  $B_1$  and  $B_3$  according to the equation

shown in Figure 2. Velocity data collection on May 24 occurred during a falling tide. These data exhibited a 12.2% weaker average  $B_2$  amplitude response and more consistent fluctuations in the beam signal than on May 23, likely a result of smaller or fewer scattering particles suspended in the water column, but no phase-wrapping. On May 24 there were obvious non-physical deviations in beam velocity magnitude between  $B_1$  and  $B_3$ , such as  $B_1$  velocity jumping by 50%–100% relative to  $B_3$  or vice-versa, likely a result of the lower beam amplitudes and hence weaker signal-to-noise ratio. Threshold velocity filtering was implemented in beam coordinates to remove these spurious velocities, followed by processing with the AGW filter. This ensured that the AGW filter could accurately and robustly estimate the standard deviation of the signal of interest before the  $u$  and  $w$  velocities were calculated.

Remote measurements of free surface velocity can be used to estimate the depth-averaged channel velocity using the velocity index  $k = U_b/U_{surf}$ , the ratio of depth-averaged to surface velocity. The velocity index is an important component of calculating volumetric discharge from surface velocity measurements (Levesque & Oberg, 2012). This ratio was derived using experimental data from Hulsing (1967) by Rantz (1982), who determined that a velocity index of  $k = 0.85$  for natural channels produced errors under ±5% of volumetric discharge. Due to the common use of the velocity index to make inferences about bulk flow from remote free surface velocity measurements (e.g., Johnson & Cowen, 2017; Kim et al., 2008; Puleo et al., 2012), our study inverted the velocity index and applied it to the depth-averaged, time-dependent vertical profile of streamwise velocity measured by the AquaDopp, to derive a surface-extrapolated velocity ( $U_{surfex}$ ) based on this in-channel data:

$$U_{surfex} = \frac{\langle U(t, z) \rangle}{k} \quad (1)$$

This relationship reflects the depth-averaged velocity estimates that would be made in a study using only remote surface velocimetry measurements with a velocity index, that is, that the depth-averaged velocity is 85% of the surface velocity. Equation 1 also provides a more robust estimate of the idealized surface velocity in the absence of wind than AquaDopp velocity measurements in the bin nearest the surface, which often suffers from noise and dropouts in the data collected for this study.

### 2.3. Drone-Based Image Collection

The drone used for this experiment was a DJI Matrice 600 Pro that hovered at approximately 30 m over the tidal channel. The drone was fitted with a Gremsy S1 gimbal carrying a Micasense Altum six-band imager, which includes a thermal infrared microbolometer sensor (specifications in Table 1).

Five repeated drone flights were launched from the end of the access road just west of the weather station adjacent to the combined channel of Franklin and Santa Monica Creeks shown in Figure 1. Imagery of tidal flow was collected from the hovering drone for approximately 10 min per flight at this point along the channel. The spatial coverage of the drone field of view relative to the in-channel AquaDopp is shown in Figure 3. The Micasense imageprocessing toolbox in Python was used to align the six imagery bands, correct for lens distortion, and upsample the lower-resolution thermal band to the resolution of the visible bands (2,064 × 1,544 pixels) (McAllister et al., 2024).

As shown in Table 1, the Micasense Altum thermal band has a relatively small number of pixels, leading to a very coarse spatial resolution (19.6 cm per pixel on average during this experiment). However, patterns detected on the water surface visible in the thermal infrared drone images taken during each flight still presented a trackable

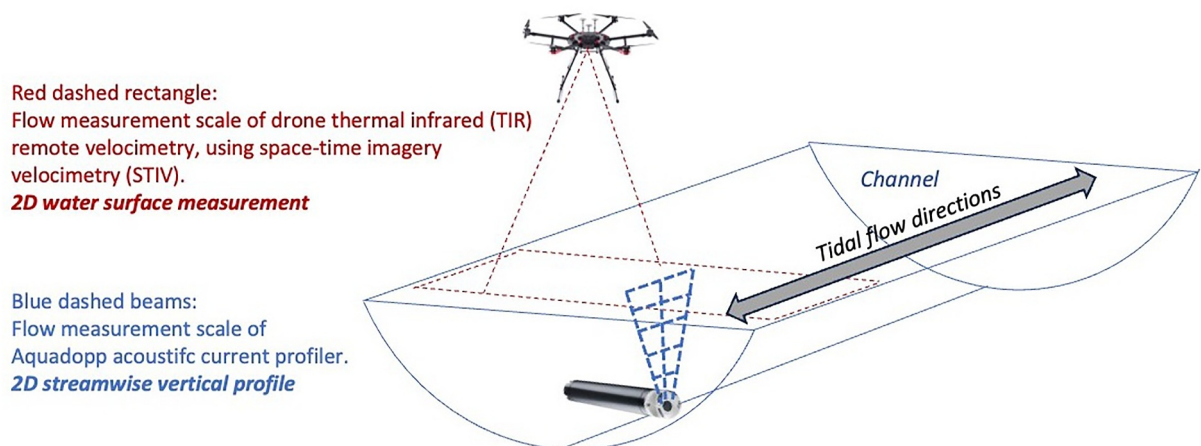


**Figure 3.** Experimental schematic showing orientation and surface extent of AquaDopp measurement beams in blue relative to drone imagery FOV in red. Actual drone FOV included portions of both channel banks for each flight. Figure not to scale.

signal for the STIV pattern tracking algorithm used for image velocimetry (Section 2.5). Since STIV only requires relative differences in intensity or value between pixels in any type of imagery to produce trackable patterns, thermal infrared pixel intensities were not converted to temperature in this experiment. STIV was conducted for each flight using a subset of each thermal infrared image in the flight time series that was located directly above the in-channel AquaDopp, thereby measuring water velocity in the same area of the channel using both the drone-based and in-channel methods to enable direct comparisons between the two.

To create the unified  $x$ -axis aligning pixel columns in the drone images with the AquaDopp's planar beam orientation shown in Figure 3, the location and orientation of the AquaDopp were identified in an RGB image assembled from the aligned bands of the first stationary image in each flight. This image was rotated by an angle which aligned the vertical pixel columns in the image with the AquaDopp  $x$ -axis, and all subsequent images in each flight's time series were rotated by this angle. The location of the AquaDopp head in the rotated image was set as the  $x$  coordinate origin for each flight, as shown in Figure 4.

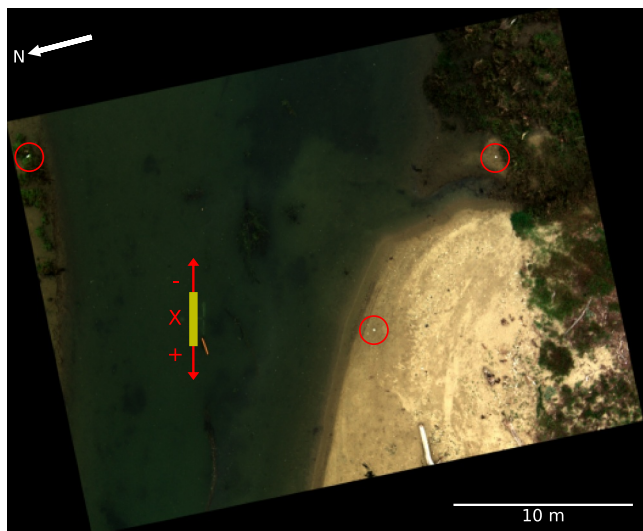


**Figure 4.** Three-band RGB drone image collected during flight C with the  $x$ -axis located directly over the AquaDopp velocity measurement head. The positive  $x$ -direction denotes tidal outflow, while  $x < 0$  denotes tidal inflow. The translucent yellow region shows the location of  $u$ -velocity measurements along the  $x$ -axis: both the image pixel coordinates sampled in STIV and the surface extent between AquaDopp beams 1 and 3. Images were rotated so that the AquaDopp  $x$ -axis was parallel to pixel columns in images. Ground control points visible during this flight are circled in red. True north relative to the rotated image is shown at top left, with the spatial scale at bottom right. An orange recovery float is visible to the right of  $x$ -axis.

#### 2.4. Georeferencing and Stabilization of Drone Images

Five GCPs consisting of rocks wrapped in aluminum foil for thermal band visibility were placed along the banks of the tidal channel at CSMR, and their center positions were averaged over 10 min per GCP with an InertialSense GPS. To georeference the aligned and rotated images, the GCPs visible in each flight were identified and the ratio of the distance between GCPs in pixel space (from the first stationary image in the flight) and physical space (from the GPS measurements) was averaged for all GCP pairs to derive a pixels-per-meter ratio for each flight, which was assumed constant across the image due to the nadir viewing angle. The location of the aligned AquaDopp and STIV  $x$ -axis was stabilized from image to image by tracking the displacement of a GCP from image to image caused by drone motion during the hover. The  $x$  coordinate origin overlying the AquaDopp was corrected for each image using the displacement of the GCP from the previous frame in the hover. Therefore, the STIV coordinate origin location was maintained over the AquaDopp head despite any drone movement.

The performance of this GCP displacement method to correct for drone motion was compared to a method using the GPS data recorded when each photo was taken (Pirelli, 2019), shown in Figure 5. The GPS method estimates the displacement of the four image corners in physical space due to drone motion between each image in the time series, and these four corner

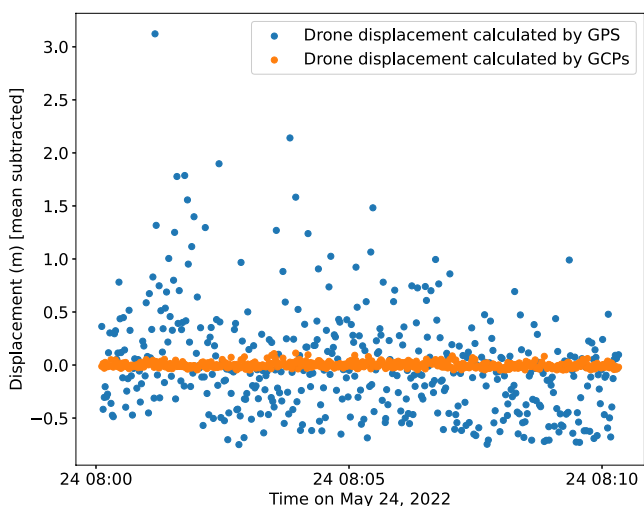


**Figure 5.** Comparison of image stabilization methods for flight C. Each point shows the respective method's estimated horizontal displacement of the drone from the previous image based on a stationary ground location (GCP or the previous image's corner pixel locations) in meters. Displacements were calculated as distance magnitude from the previous timestep without accounting for direction, and means were subtracted from each time series for comparison.

Dopp's acoustic measurement plane was oriented in an along-stream direction with the beam orientation denoted as the yellow line in Figure 4, and the one-dimensional STIV method most closely recreates this measurement axis from the drone images.

displacements were averaged to one displacement value at each timestep. The DJI drone's standard internal GNSS unit was set to GPS lock mode for all flights, but no real-time kinematic (RTK) base connection was set up. GPS  $x, y$  accuracy ranged from 0.78 to 1.02 m over this flight, and this range is of the same order of magnitude as the random noise exhibited in the GPS signal in Figure 5. In the absence of RTK-level GPS accuracy during a drone flight, this comparison indicates that the GCP-based drone motion tracking method used herein is potentially more robust to the effects of small drone motions than the GPS method, directly correcting space-time diagram origin coordinates based on the apparent motion of a GCP from image to image. This accuracy is reflected in the standard deviation of the drone displacements calculated by the GCP method (2.9 cm, or 1.8 pixels before conversion) compared with the much larger standard deviation of displacements from the GPS method (49.6 cm), suggesting that the GPS position is dominated by random error while the GCP displacement approach appears more reflective of the drone's actual drift.

## 2.5. Space-Time Image Velocimetry (STIV)

We chose STIV for velocimetry analysis because (a) Microbolometer infrared measurements generally exhibit only modest signal-to-noise ratio when imaging water in the environment, and STIV is one of the most robust quantitative imaging approaches to determining the mean velocity field from relatively noisy imagery (Lu et al., 2023; Torres-Rua, 2017); (b) the Aqua-

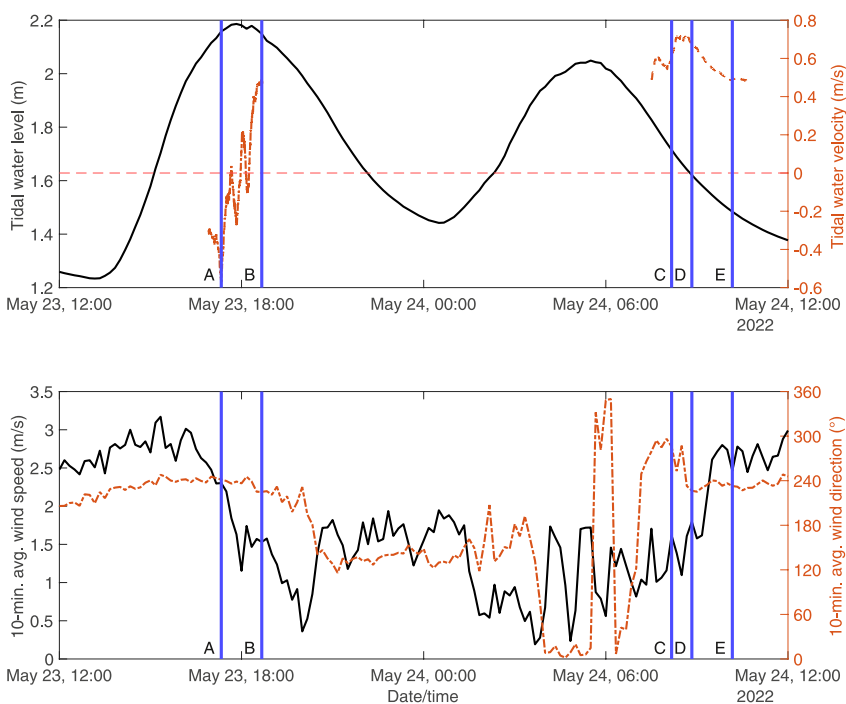


**Figure 6.** Tide and wind conditions during the experiment (conducted May 2022). Top: Relative tidal elevation (black solid) and 10-min averaged surface-extrapolated tidal velocity from the deployed AquaDopp ( $U_{\text{surfex}}$ , red dashed) over two experiment days. Red dashed velocity zero-axis highlights the sign of tidal velocity denoting flow direction. Bottom: Average wind speed (black solid) and direction (red dashed) over the same time period. Timing of five 10-min drone flights denoted by blue vertical lines on both plots, letters next to lines denote flight.

The extent of the  $x$ -axis sampled from images in STIV was determined by calculating the physical distance between the diverging  $B_1$  and  $B_3$  AquaDopp beams at the water depth identified in the vertical  $B_2$  beam during each flight using the geometry of the AquaDopp head shown in Figure 2. Then this physical distance between the AquaDopp beams was converted to pixels using the pixels-per-meter ratio calculated for each flight using the GCPs. The length of the  $x$ -axis is therefore a function of water depth: when the water depth was greater, the oblique AquaDopp beams diverged farther before reaching the surface, and more of the  $x$ -axis fell between the beams, so a larger set of pixels along the  $x$ -axis was sampled for STIV.

The pixel extent of the  $x$ -axis was centered on the AquaDopp head coordinate  $x = 0$ , and this column of pixels was appended to the space-time diagram at each timestep from the same pixel location in the rotated and stabilized image time series. The mean pixel intensity was subtracted from each individual thermal image before the column of pixels along the STIV  $x$ -axis was added to the space-time diagram to correct for changes in the microbolometer camera's temperature, which can cause changes to the global pixel intensity from image to image. The Micasense imageprocessing toolbox was used to import and align the six-band imagery (McAllister et al., 2024). This workflow was designed to ensure the most precise possible comparison between remote and in situ velocity measurements rather than to estimate a synoptic surface velocity field.

The pixel intensity gradient across the space-time diagram was measured by integrating the two-dimensional autocorrelation in a polar coordinate system; the maximum of this integral ( $\phi$ ) represents the angle of highest autocorrelation, which can be converted to a velocity using the pixels per meter ratio and framerate. These gradient features' angles represent velocities based on the units of the space-time diagram axes—distance traveled over a specific time:

$$U_{STIV} = \frac{S_x}{S_t} \tan \phi \quad (2)$$

where  $S_x$  is the physical length scale per pixel (1.6 cm/pix for flight C),  $S_t$  is the time scale per pixel (or framerate $^{-1}$ , 1.34 s/pix for flight C), and  $\phi$  is the maximum of the two-dimensional autocorrelation integral (Fujita et al., 2019). The tangent of the angle  $\phi$  gives a distance to time ratio or velocity in pixels, which is converted to meters per second by multiplying by the distance and time scales  $S_x/S_y$ . This process was repeated in 20 overlapping square sections of the space-time diagram, which were evenly distributed along the entire time axis to resolve changes in the STIV velocity measurement during each flight. The dimensions of these square sections were set by the  $x$ -axis pixel length scale for each flight's space-time diagram, ensuring that velocity calculations were made along the same spatial scale as the in-channel  $U_{surfex}$  velocity measurements.

This project's implementation of STIV was designed to enable as direct a comparison as possible with the in situ AquaDopp measurements, rather than demonstrating an optimized example of this velocimetry method. To make synoptic surface velocity measurements, many STIV search lines would be sampled across images of the water surface, and each search line's orientation could be optimized to lie parallel to the local flow direction (Han et al., 2021; Legleiter, Kinzel, Engel, et al., 2024). In our project, the STIV  $x$ -axis orientation was simply set by the orientation of the AquaDopp's  $x$ -axis in the tidal channel, and only one search line was sampled because the primary objective was a localized comparison between the remote STIV and in situ AquaDopp measurements. Several user-friendly applications and toolboxes exist for surface velocimetry using drone imagery (e.g., Hydro-STIV used by Biggs et al., 2022; Legleiter & Kinzel, 2023), and our goal in this project was to assess the need to consider wind stress effects on the surface velocity fields produced by these existing software tools.

## 2.6. Tide and Wind Conditions

CSMR maintains a meteorological station that measures tidal elevation and wind speed and direction every three seconds (0.3 Hz), recording the average, minimum, maximum and standard deviation of these metrics in 10-min intervals. Tidal elevation is measured using a pressure transducer in the tidal channel bed adjacent and connected to the meteorological station tower. The tidal stage over the course of the experiment is shown in the top plot of Figure 6. Meteorological station wind data come from an anemometer positioned 9.75 m above ground level, with wind direction angles referenced to true north (UCNRS, 2022) and defined as the direction from which the wind originates. Average wind speeds were less than 5 m/s for all flights during the experiment, as shown in the bottom plot of Figure 6. The location of the meteorological station relative to the experiment location is shown in

**Table 2**

Wind Velocity and Direction Average and Standard Deviation ( $\sigma$ ) Values From the CSMR Meteorological Station During Each Flight

Flight	Wind $\bar{U}_{10}$ (m/s)	Wind $\sigma_{U_{10}}$ (m/s)	Wind angle from N	Wind angle $\sigma$
A	2.30	0.34	242°	7°
B	1.53	0.31	225°	10°
C	1.62	0.36	286°	17°
D	1.80	0.33	227°	10°
E	2.46	0.30	233°	9°

Figure 1. The drone was launched and operated within roughly 50 m of the meteorological station during this study.

This experiment was conducted on two mostly cloudy days at the start of coastal California's summer low cloudiness season, which is caused by persistent temperature inversions associated with the season of maximum lower tropospheric stability (Clemesha et al., 2016). All flights were conducted during sea breeze conditions, with average winds coming off the Santa Barbara Channel from an approximately southwest-west (225°–270°) direction (Table 2).

Data from the meteorological station were used to calculate surface wind stress during each flight. Because the elevation of the meteorological station anemometer is within 0.25 m of 10.00 m from the ground, and the meteorological station is located on the bank of the tidal channel approximately one m above the water level (which fluctuates on the order of one m with the tidal stage as shown in Figure 6), the meteorological wind speed was used directly as an approximation for  $U_{10}$ .

The wind drag coefficient at the water surface  $C_{10}$  was determined using a least square fit for  $U_{10} < 5$  m/s from Wüest and Lørke (2003):

$$C_{10} = 0.0044U_{10}^{-1.15} \quad (3)$$

The parallel component of the wind stress,  $\tau_{||}$ , at the water surface relative to the  $x$ -axis was calculated using this drag coefficient and the anemometer wind speed estimate for  $U_{10}$ :

$$\tau_{||} = \rho C_{10} U_{10}^2 \cos \theta \quad (4)$$

where  $\rho$  is the density of seawater (1,026 kg/m<sup>3</sup>) and  $\theta$  is the angle between the  $x$ -axis and the average wind direction.  $\tau_{||}$  is positive in the same direction as the tidal flow and negative in the opposite direction. The orientation of the rotated aligned images relative to north and the wind direction was determined using the physical locations of GCPs visible in each set of rotated images.

### 3. Results

Trackable thermal signatures were present in the images collected during each flight. Figure 7, a typical image, shows pixel intensity variations on the water surface that are advected along the channel from image to image in the time series. An animation showing the time series of thermal images used for pattern tracking is also available in the Supporting Information S1.

For each flight, a space-time diagram was assembled by sampling pixels along the  $x$ -axis overlying the measurement beams of the AquaDopp, which were added to the diagram at each timestep. A sloping gradient was clearly visible across space-time diagrams for all five flights, as shown in Figure 8.

#### 3.1. Uncertainty Associated With Time Synchronization Between Velocity Measurements

To assess the difference between the drone-based and in-channel velocity measurements during each flight, 20 overlapping STIV velocity measurements ( $U_{STIV}$ ) from each flight's space-time diagram were compared with 20

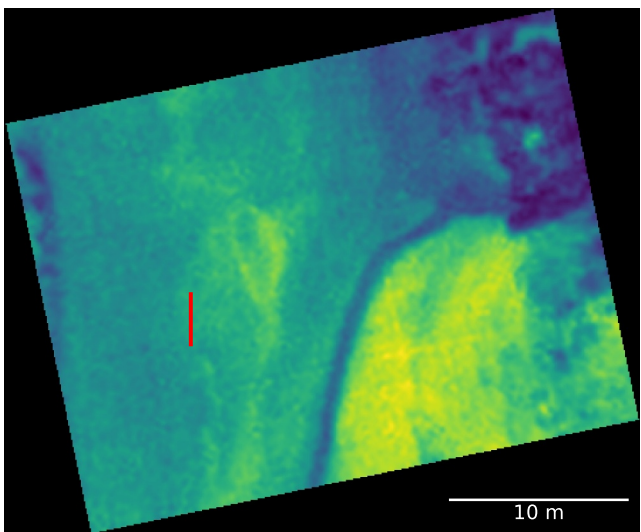


**Figure 7.** Rotated infrared thermal image from flight C corresponding to the same timestep as the RGB image in Figure 4, upsampled to the resolution of the visible light bands. Pseudocolor scale shows differences in relative pixel intensity in the thermal infrared band, not converted to real temperature. Location of the  $x$ -axis sampled by STIV overlying the AquaDopp is shown in red. An animated version of this figure showing the stabilized  $x$ -axis location is available in the Supporting Information S1.

corresponding surface-extrapolated velocity ( $U_{\text{surfex}}$ ) measurements from the AquaDopp averaged over the time duration represented by each STIV measurement. A time series of these two velocity signals is shown in Figure 9. The AquaDopp was synchronized to computer time during pre-deployment programming.

The Altum camera's internal clock was not synchronized to computer time on May 23. Hover period timestamps and image framerate during flights A and B were derived from the drone's internal GPS log by identifying the period of constant maximum drone elevation and near-zero velocity, and dividing the number of stationary images by this GPS time duration. Flight B's GPS-derived start and end timestamps are within one to 3 seconds of hover times noted in the field using cell phone time. On May 24 a meteorological mast was mounted on the drone which triggered recording of GPS-derived accurate timestamps for each image collected during flights C, D, and E. Image timestamps allowed for a direct comparison between individual STIV velocity measurements and corresponding periods of the AquaDopp surface-extrapolated velocity signal.

Nortek, the AquaDopp manufacturer, defines the uncertainty as 1% of the measured velocity value  $\pm 0.5$  cm/s for the AquaDopp HR model used in this study (NortekAS, 2017). Based on the velocity range for flight C shown in Figure 9 this would yield a maximum uncertainty of  $\pm 1.49$  cm/s.

### 3.2. Coordinate System and Sign of Velocity Measurements

For streamwise water velocities in this coordinate system, positive velocities denote outflow from the estuary, and negative velocities denote tidal inflow.

The difference in velocity  $U_{\Delta}$  between the STIV velocity measurement  $U_{\text{STIV}}$  and surface-extrapolated AquaDopp velocity measurement  $U_{\text{surfex}}$  was calculated accordingly:

$$U_{\Delta} = \text{sign}(U) * |U_{\text{STIV}} - U_{\text{surfex}}| \quad (5)$$

where  $\text{sign}(U)$  is the sign function:

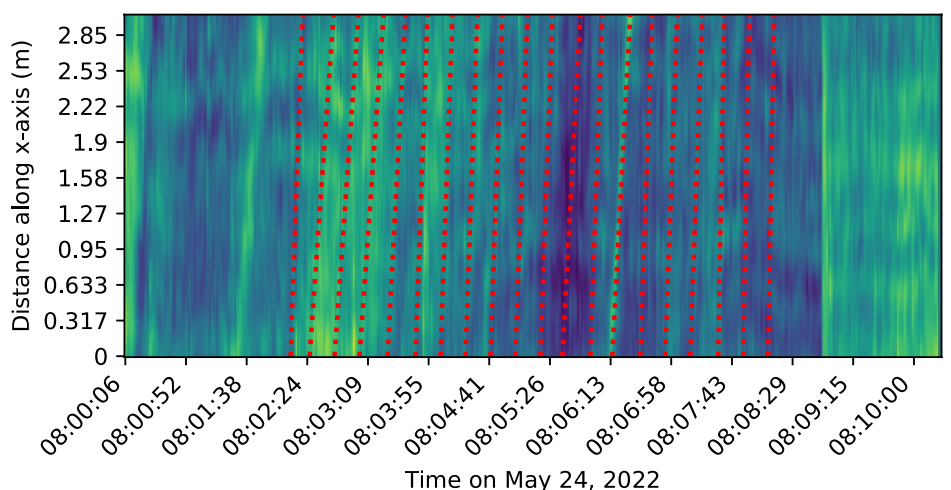


**Figure 8.** Space-time diagram for flight C, assembled by sampling one spatial column of pixels from the  $x$ -axis in each image during the 10-min hover timeseries. 20  $\phi$  angles detected from the space-time diagram are shown at their centered locations within the overlapping square windows of the diagram which were analyzed to derive each angle.

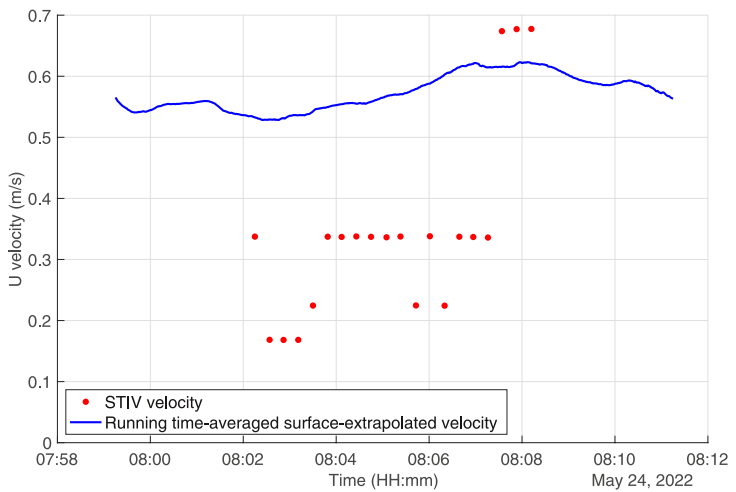


**Figure 9.** Surface-extrapolated velocity ( $U_{surfex}$ , blue line) from the AquaDopp running-averaged over the same duration as 20 flight C STIV velocity measurements ( $U_{STIV}$ , red points) generated from the 20 detected  $\phi$  angles shown on the space-time diagram in Figure 8 according to Equation 2.

$$\text{sign}(U) = \begin{cases} 1 & \text{if } |U_{STIV}| > |U_{surfex}| \\ -1 & \text{if } |U_{STIV}| < |U_{surfex}| \end{cases} \quad (6)$$

$U_{STIV}$  and  $U_{surfex}$  had the same sign for all flights except for flight B: the surface-extrapolated AquaDopp velocity measurement direction had switched to outgoing from flight A, but the STIV velocity measurement direction remained incoming, as shown in Table 3. For flight B,  $|U_{STIV}| < |U_{surfex}|$ , and this flight had the largest velocity difference due to the difference in sign between the two velocities. The effect of wind stress parallel to the  $x$ -axis on the difference  $U_\Delta$  between STIV velocity measurements and surface-extrapolated AquaDopp velocity measurements is shown in Figure 10.

#### 4. Discussion

Wind direction relative to the tidal flow direction played a clear role in the sign and magnitude of the drone-based STIV velocity measurements relative to the surface-extrapolated in-channel AquaDopp velocity measurements. Winds were approximately out of the west ( $270^\circ$ ) or southwest ( $225^\circ$ ) off the Santa Barbara Channel during all flights (Table 2), roughly aligning with the direction of incoming tide in the channel where the experiment was conducted. During flight A when the parallel wind stress ( $\tau_\parallel$ ) was aligned with the direction of the incoming tide,

**Table 3**  
*AquaDopp Surface-Extrapolated and Drone-Based STIV Velocity Measurements, and Two Metrics of Wind Effects on Surface Velocity: Angle Between Wind Direction and Measured Flow Direction, and the Wind Stress Component Parallel to the Flow Direction Along the  $x$ -Axis During Each Flight*

Flight	AquaDopp $\bar{U}_{surfex}$ (m/s)	Drone $\bar{U}_{STIV}$ (m/s)	Wind angle from $\bar{U}_{surfex}$ direction	Parallel wind stress $\tau_\parallel$ (Pa)
A	-0.56	-0.61	-42°	6.9
B	0.49	-0.12	123°	-3.6
C	0.57	0.35	180°	-6.8
D	0.66	0.29	124°	-4.2
E	0.49	0.36	127°	-5.9

*Note.* Note that the in-channel surface-extrapolated tidal velocity changed directions between flights A and B but the STIV velocity measurement direction remained constant.

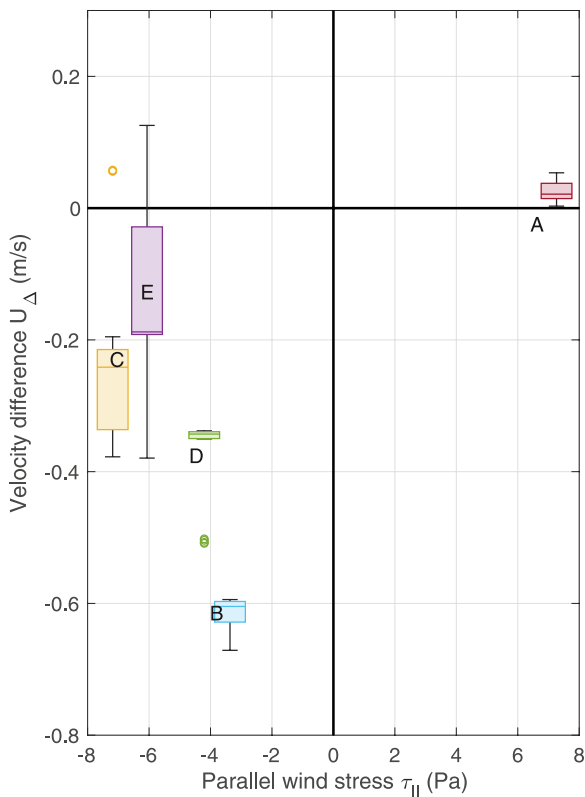


**Figure 10.** Parallel wind stress ( $\tau_{\parallel}$ ) effect on calculated difference ( $U_{\Delta}$ ) between STIV velocity measurement ( $U_{STIV}$ ) and surface-extrapolated velocity measurement ( $U_{surfex}$ ) for five flights. Individual boxplots summarize 20 time-synchronized comparisons between the two velocity measurements, showing median, first and third quartile box, largest non-outlier whiskers based on interquartile range, and any individual outliers. The vertical axis intercept  $U_{\Delta} = 0$  denotes that the two velocity measurements were equal.

calculations are feasible over shorter timescales within a given 10-min flight, such as estimating the wind-driven water surface velocity component.

Similar to the decoupled unsteadiness of wind stress and tidal velocity during a single flight, wind and tidal flow directions also differ across diurnal timescales visible between flights. For example, flight B has a significantly larger  $U_{\Delta}$  magnitude in Figure 10 than the four other flights due to the difference in direction between the two velocity measurements. This outlier could be explained by flight B's timing relative to the tidal cycle and diurnal wind patterns typical of coastal regions. For much of the 6 hour period preceding flight B, the wind had been blowing roughly onshore at 2.5–3 m/s, while the tide was steadily rising (Figure 6), resulting in a tidal flow roughly aligned with the prevailing wind. This alignment between the afternoon sea breeze direction and rising tidal flow direction could have contributed to the high STIV velocity measurement magnitude for flight A relative to the four other flights shown in Table 3. When the tide crested between flights A and B, the depth-averaged flow direction reversed while the wind direction remained relatively constant, and this upstream surface momentum flux due to wind stress would have taken time to dissipate. It appears that during flight B, which was conducted less than an hour after high tide, the wind was still blowing the surficial skin layer of the water column upstream while the rest of the water column had switched directions to an outgoing tide. Presumably, an overnight outgoing tide could be similarly accelerated by aligned wind stress of an offshore nighttime land breeze, highlighting the potential constructive or destructive relationship between wind direction and tidal velocity depending on how

the mean STIV velocity measurement was higher than the surface-extrapolated in-channel AquaDopp velocity measurement, as shown in Table 3. For all other flights, when the parallel wind stress was opposite to the tidal outflow, the mean STIV velocity measurement was lower than the surface-extrapolated velocity. In fact flight B, which occurred soon after the tidal flow had changed direction from incoming to outgoing as shown in Figure 6, actually appeared to still have an incoming tidal velocity direction in the STIV surface measurement. This difference in measured flow direction is an important result for remote measurements of surface velocity with relatively slow ( $<1$  m/s) or unsteady flows when wind stress is a factor. As shown in Figure 10, the velocity differences ( $U_{\Delta}$ ) between the two measurement methods can be of the same order as the surface-extrapolated “water-truth” in-channel velocities measured by the AquaDopp ( $U_{surfex}$ ), representing a significant potential source of error if the remote STIV velocity measurement was assumed to be indicative of the bulk flow velocity under these wind and flow conditions.

#### 4.1. Physical Causes of Time-Varying Velocity Differences

The range of individual velocity measurement differences ( $U_{\Delta}$ ) across the five flights shown in Figure 10 are on the order of 5–50 cm/s, much larger than the AquaDopp's maximum uncertainty for flight C of 1.5 cm/s. This range could be partially explained by differing timescales of unsteadiness between the in-channel flow velocity and the wind speed and direction. The  $U_{surfex}$  timeseries in Figure 9 is running-averaged over a timescale greater than 4 minutes to match the time-averaging inherent to the STIV velocity measurement method, while the non-averaged  $U_{surfex}$  velocity signal fluctuates within the same or greater bounds on the order of seconds. Similarly, the met station wind data are 10-min average values, and the wind speed and direction standard deviation ( $\sigma$ ) values in Table 2 reflect the unsteadiness of surface wind stress during each flight. While local wind stress likely has some effect on water velocity throughout the water column, fluctuations in surface wind stress are decoupled from tidal flow dynamics, resulting in changing velocity differences during a single flight. Wind duration and fetch, which varies greatly with wind direction at the study site, have a high impact on the wind-driven transport of water surfaces (Veron & Melville, 2001). The 10-min average wind data available for this study therefore limits what wind stress

these two diurnal cycles align on a given day. This finding further emphasizes the complex interacting processes that modulate surface wind stress effects in the intertidal zone, as past studies have shown that expected air to sea momentum fluxes caused by surface wind stress in coastal areas can deviate significantly from open ocean parameterizations due to other nearshore processes such as horizontal current shear, depth-limited wave breaking, and decreased wave celerity in shallow water (e.g., Ortiz-Suslow et al., 2015).

#### 4.2. Measurement Uncertainty and Data Quality

Tradeoffs between the spatial and temporal scales of drone imagery used for STIV analysis shaped this study's methods. Using flight C as a typical example, the characteristic length scale of the area shown in drone images during the hover was 23.7 m in the streamwise direction (along the short image axis) and 31.6 m in the cross-channel direction (along the long image axis), using the pixel to meter conversion derived from the GCP coordinates. As shown in Figure 7, the region of pixels sampled in STIV relative to the overall image dimensions is small, and a lower hover altitude would have enabled higher resolution space-time diagrams with a larger number of pixels in the direction of the flow and smaller pixel footprints. The conservative choice of a 30 m target hover altitude was based on uncertainty regarding the water depth and AquaDopp beam divergence distance, as well as a lack of a live feed from the Altum camera. The frame rate of the collected images was somewhat variable, as the Altum camera was set to record at 1 Hz while its recommended maximum frame rate is 0.67 Hz. As a result, the imaging frequency was limited by the write speed of the camera hardware, with a typical framerate of approximately 0.75 Hz across the five flights. Therefore, a lower hover altitude could have introduced other measurement challenges by increasing the pixel length scale of apparent pattern motion between frames, demonstrating the tradeoff between spatial resolution and frame rate that bounded this experiment's methods.

The second major reason likely explaining the range in velocity differences within individual flights in Figure 10 is the angular sensitivity of the STIV method applied to data collected at a slower-than-optimal framerate. Due to the pixel length of the  $x$ -axis that overlaid the AquaDopp measurement beams at the surface (192 pixels for flight C), it was not feasible to resolve the two-dimensional autocorrelation's polar integral in increments smaller than one degree, as some fractional increments of a degree did not intersect with any pixels in this relatively small grid. Despite the drone flying conservatively high, the upsampled thermal band pixel footprint was still a reasonably high-resolution 1.6 cm/pix. Combined with the Altum's sub-1 Hz framerate, this fine spatial scale yielded large apparent motion of thermal features along the  $x$ -axis from image to image. This produced steeper than desired pixel intensity gradients in the space-time diagrams, resulting in at least one polar integral maxima ( $\phi$ ) at the steepest possible angle ( $\pm 89^\circ$ ) in flights A, C and E. Angles this steep are less than ideal for STIV velocity measurements due to the sensitivity of the tangent function at near-right angles, since  $\tan \pm 90^\circ$  is asymptotic to infinity, and STIV's velocity estimation error is lowest for angles  $\phi = 45^\circ$  (Fujita et al., 2019; Legleiter, Kinzel, Engel, et al., 2024). In Figure 9, the four STIV velocity measurement increments correspond to  $\phi = 86\text{--}89^\circ$ , highlighting this method's lack of precision at steep angles. However, the trend described by the individual STIV velocity measurements does follow the surface-extrapolated velocity with peaks and valleys in the same parts of the flight C time series, and the same was true for flight E within the same  $4^\circ$  range of  $\phi$  angles.

Flight A in particular would have benefited from a faster framerate, as  $\phi$  was  $\pm 90^\circ$  for all STIV measurement windows, with the second highest integral maxima at  $-89^\circ$ . Therefore, the underestimate  $\phi = -89^\circ$  was assumed for all STIV velocity measurements. However, this underestimate still produced a larger  $U_{STIV}$  velocity than the contemporaneous  $U_{surfex}$  velocity, resulting in a positive  $U_\Delta$  value for flight A despite this flight occurring during a strong peak in the  $U_{surfex}$  incoming tidal velocity (Figure 6). The actual STIV velocity measurement magnitude was almost certainly larger than the  $-0.61$  m/s measurement at this framerate (Table 3). A more accurate  $U_{STIV}$  measurement would likely make  $U_\Delta$  more positive and push the spread of velocity comparisons for flight A higher in Figure 10, further strengthening the positive relationship between  $\tau_{||}$  and  $U_\Delta$  visible in this figure. Therefore, the STIV velocity measurements for flight A exhibit a higher uncertainty than other flights, but the clear signs of negative directional bias in this flight's STIV analysis maintain a strong causal relationship between wind stress and apparent surface flow velocity based on the overall results of this study.

Differences in data quality were apparent across the tidal cycle for both drone images and AquaDopp velocity measurement data. In terms of thermal resolution of trackable features in the imagery, differences in image quality between flights are influenced by a number of environmental factors affecting the imaging sensor such as air temperature and wind (Legleiter, Kinzel, Dille, et al., 2024; Lewis et al., 2018), as well as the thermal signal on the

water surface. For example, the scale of turbulent thermal structures can vary significantly across the tidal cycle (Zappa et al., 2003), which could present a challenge in successfully implementing this method in an unbiased and consistent way at any tidal stage. Differences in infrared signal-to-noise ratio could also have contributed to spurious peaks in the two-dimensional autocorrelation polar integral for some flights' space-time diagrams, despite normalizing the integral by the number of pixels within each degree bin. The integral maxima ( $\phi$ ) for flights D and E were largely biased to pixel rows and columns due to apparent fixed pattern noise, with the resulting 0° or 90° angles representing non-physical velocities of zero or infinity. This bias was eliminated by constraining the valid range of  $\phi$  angles for flights D and E to ±1–89°, and the resulting  $\phi$  time series fluctuated between 84 and 89°, similar to the range in flights B and C which did not require such bias correction. In summary, there were two sources of right-angle bias across three flights, with flight A requiring bias correction due to an insufficient framerate for the velocities measured, and flights D and E requiring bias correction due to fixed pattern noise in the space-time diagram. Changes in acoustic velocity profiler echo intensity between ebb and flood tide have been observed in other studies due to differences in passive scalar concentration (Dugan & Piotrowski, 2012). Differences in the intensity of the AquaDopp signal response were apparent between the two deployments in this experiment which occurred at different tidal stages, with an average normalized amplitude response of 55.6% on May 23 during the rising and cresting tide, and an average response of 43.4% on May 24 during the falling tide. This lower amplitude response on day two could partially explain observed relative noisiness of May 24th's AquaDopp data in this study.

#### 4.3. Implications for Image-Based Surface Velocity Measurements

Measurements near the water surface using in situ instruments, such as acoustic velocity profilers, are challenging. Acoustic velocity measurements near the free surface often exhibit a reflectance band of acoustic signal interference which can lead to less accurate measurements (González et al., 1996), and placing instruments in the channel also disturbs the flow being measured. Remote sensing velocimetry techniques, such as the drone-based STIV method presented here, keep people out of harm's way and can produce distributed surface velocity measurements over a much wider area than acoustic current profilers. However, if the surface velocity signal being measured is significantly contaminated by wind stress, incorrect conclusions might be drawn. For example, applying a velocity index of 0.85 to the  $U_{STIV}$  velocity measured from the drone during flight B would yield a depth-averaged velocity of −0.11 m/s, denoting an incoming tide. However, in the tidal elevation in Figure 6 as well as the sign of the AquaDopp  $U_{surfex}$  velocity measurement relative to flight A, it is clear that flight B occurred after the tidal flow direction had turned to outgoing. Therefore, one could easily draw the wrong conclusion from flight B's STIV results alone, and this appears to be due to the surface wind stress in the incoming tide direction. Furthermore, the substantial spread of individual  $U_{\Delta}$  values within multiple flights in Figure 10 shows that decoupled surface wind stress fluctuations and bulk velocity fluctuations present another potential source of error in estimating bulk velocity from surface velocity.

Importantly, across multiple flights the velocity differences ( $U_{\Delta}$ ) between the two measurement methods are of the same order as the surface-extrapolated "water-truth" in-channel velocities measured by the AquaDopp ( $U_{surfex}$ ), and in one of five test flights the measured direction of the compared velocities was opposite. These results demonstrate that surface wind stress relative to the magnitude of bulk flow velocity is an important factor in accurately estimating bulk velocity and discharge from remote surface water velocity measurements. This finding is a reminder that differences between remote sensing velocity measurements and in-channel acoustic velocity measurements reflect the different physical processes observed by each method; acknowledging this difference is critical, as remote sensing techniques are increasingly used to infer in situ velocities. Ongoing technological advances such as drone-mounted wind speed anemometers and growing access to velocimetry software tools present additional methods to further explore the focus of this study. Additional studies of wind stress effects on surface velocimetry applications are necessary to develop methods that account and correct for wind stress when making remote measurements of water velocity in the environment.

#### Acronyms

ADCP	acoustic Doppler current profiler
PIV	particle image velocimetry

FOV	field of view
GCP	ground control point
STIV	space-time image velocimetry
IR-QIV	infrared quantitative image velocimetry
CSMR	Carpinteria salt marsh reserve
AGW	adaptive Gaussian window
RGB	red-green-blue
RTK	real-time kinematic

## Data Availability Statement

Publicly accessible data used in this project such as UC Natural Reserve System meteorological station data (UCNRS, 2022) and USGS stream gauge data (USGS, 2022) are cited in the bibliography, along with published software implemented in analysis (Cowen, 2006; McAllister et al., 2024; Pirelli, 2019).

Code and data needed to reproduce results from this study can be found in a dedicated Cornell University Library eCommons Repository (Heberlein et al., 2025).

## Acknowledgments

This work was performed (in part) at the University of California Natural Reserve System Carpinteria Salt Marsh Reserve (UCNRS, 2023, <https://doi.org/10.21973/N3X08Q>), and we are grateful to CSMR Director Dr. Andrew Brooks for his support of this project. We gratefully acknowledge the support of the Cornell Atkinson Center for Sustainability, the United States Geological Survey (G23AP00025-00) and Cornell University in supporting Mr. Heberlein, Dr. Schweitzer and Prof. Cowen. Grants from the Zegar Family Foundation (SB200109, SB220237) are gratefully acknowledged as a source of support for Dr. Morgan and Prof. Taylor.

## References

- Al-mamari, M. M., Kantoush, S. A., Kobayashi, S., Sumi, T., & Saber, M. (2019). Real-time measurement of flash-flood in a Wadi area by LSPIV and STIV. *Hydrology*, 6(1), 27. <https://doi.org/10.3390/hydrology6010027>
- Ansari, S., Rennie, C. D., Jamieson, E. C., Seidou, O., & Clark, S. P. (2023). RivQNet: Deep learning based river discharge estimation using close-range water surface imagery. *Water Resources Research*, 59(2), e2021WR031841. <https://doi.org/10.1029/2021WR031841>
- Biggs, H. J., Smith, B., Detert, M., & Sutton, H. (2022). Surface image velocimetry: Aerial tracer particle distribution system and techniques for reducing environmental noise with coloured tracer particles. *River Research and Applications*, 38(6), 1192–1198. <https://doi.org/10.1002/rra.3973>
- Bruner, S. E., Zappa, C. J., Anderson, S. P., & Dugan, J. P. (2016). Riverine skin temperature response to subsurface processes in low wind speeds. *Journal of Geophysical Research: Oceans*, 121(3), 1721–1735. <https://doi.org/10.1002/2015JC010746>
- Chickadel, C. C., Horner-Devine, A. R., Talke, S. A., & Jessup, A. T. (2009). Vertical boil propagation from a submerged estuarine sill. *Geophysical Research Letters*, 36(10), L10601. <https://doi.org/10.1029/2009GL037278>
- Clark, R., & O'Connor, K. (2019). A systematic survey of bar-built estuaries along the California coast. *Estuarine, Coastal and Shelf Science*, 226, 106285. <https://doi.org/10.1016/j.ecss.2019.106285>
- Clemesha, R. E. S., Gershunov, A., Iacobellis, S. F., Williams, A. P., & Cayan, D. R. (2016). The northward March of summer low cloudiness along the California coast. *Geophysical Research Letters*, 43(3), 1287–1295. <https://doi.org/10.1002/2015GL067081>
- Cowen, E. A. (2006). Agw\_filter.m [Software]. Retrieved from [https://github.com/eacowen/AGW/blob/master/agw\\_filter.m](https://github.com/eacowen/AGW/blob/master/agw_filter.m)
- Cowen, E. A., Monismith, S. G., & Monismith, S. G. (1997). A hybrid digital particle tracking velocimetry technique. *Experiments in Fluids*, 22(3), 199–211. <https://doi.org/10.1007/s003480050038>
- Detert, M. (2021). How to avoid and correct biased riverine surface image velocimetry. *Water Resources Research*, 57(2), e2020WR027833. <https://doi.org/10.1029/2020WR027833>
- Dugan, J. P., Anderson, S. P., Piotrowski, C. C., & Zuckerman, S. B. (2014). Airborne infrared remote sensing of riverine currents. *IEEE Transactions on Geoscience and Remote Sensing*, 52(7), 3895–3907. <https://doi.org/10.1109/TGRS.2013.2277815>
- Dugan, J. P., & Piotrowski, C. C. (2012). Measuring currents in a coastal inlet by advection of turbulent eddies in airborne optical imagery. *Journal of Geophysical Research*, 117(C3), C03020. <https://doi.org/10.1029/2011JC007600>
- Eder, M., Tarab, L., Martino, R., Masso, L., Patalano, A., Ragessi, M., et al. (2023). LSPIV measurements to assess the impact of a bridge on a weakly undulating flow. *Journal of Applied Water Engineering and Research*, 11(4), 512–522. <https://doi.org/10.1080/23249676.2023.2173676>
- Elmer, W. H. (2014). A tripartite interaction between Spartina alterniflora, Fusarium palustre, and the Purple Marsh Crab (*Sesarma reticulatum*) contributes to sudden vegetation dieback of salt marshes in New England. *Phytopathology*, 104(10), 1070–1077. <https://doi.org/10.1094/PHYTO-08-13-0219-R>
- Eltner, A., Mader, D., Szopos, N., Nagy, B., Grundmann, J., & Bertalan, L. (2021). Using thermal and RGB UAV imagery to measure surface flow velocities of rivers. In *The International Archives of the Photogrammetry, Remote Sensing and Spatial Information Sciences*, XLIII-B2-2021 (pp. 717–722). <https://doi.org/10.5194/isprs-archives-XLIII-B2-2021-717-2021>
- Eltner, A., Sardemann, H., & Grundmann, J. (2020). Technical note: Flow velocity and discharge measurement in rivers using terrestrial and unmanned-aerial-vehicle imagery. *Hydrology and Earth System Sciences*, 24(3), 1429–1445. <https://doi.org/10.5194/hess-24-1429-2020>
- Ettema, R., Fujita, I., Muste, M., & Kruger, A. (1997). Particle-image velocimetry for whole-field measurement of ice velocities. *Cold Regions Science and Technology*, 26(2), 97–112. [https://doi.org/10.1016/S0165-232X\(97\)00011-6](https://doi.org/10.1016/S0165-232X(97)00011-6)
- Fagherazzi, S., Hannion, M., & D'Odorico, P. (2008). Geomorphic structure of tidal hydrodynamics in salt marsh creeks. *Water Resources Research*, 44(2), W02419. <https://doi.org/10.1029/2007WR006289>
- Fairley, I., King, N., McIlvenny, J., Lewis, M., Neill, S., Williamson, B. J., et al. (2024). Intercomparison of surface velocimetry techniques for drone-based marine current characterization. *Estuarine, Coastal and Shelf Science*, 299, 108682. <https://doi.org/10.1016/j.ecss.2024.108682>

- Friedrichs, C. T., & Perry, J. E. (2001). Tidal salt marsh morphodynamics: A synthesis. *Journal of Coastal Research*, 7–37.
- Fujita, I. (2017). Discharge measurements of snowmelt flood by space-time image velocimetry during the night using far-infrared camera. *Water*, 9(4), 269. <https://doi.org/10.3390/w9040269>
- Fujita, I., Notoya, Y., Tani, K., & Tateguchi, S. (2019). Efficient and accurate estimation of water surface velocity in STIV. *Environmental Fluid Mechanics*, 19(5), 1363–1378. <https://doi.org/10.1007/s10652-018-9651-3>
- González, J. A., Melching, C. S., & Oberg, K. A. (1996). Analysis of open-channel velocity measurements collected with an acoustic Doppler current profiler. *RIVERTECH*, 96.
- Han, X., Chen, K., Zhong, Q., Chen, Q., Wang, F., & Li, D. (2021). Two-dimensional space-time image velocimetry for surface flow field of mountain rivers based on UAV video. *Frontiers in Earth Science*, 9, 686636. <https://doi.org/10.3389/feart.2021.686636>
- Heberlein, E. T., Mayes, M., Morgan, B. E., Taylor, K. K., Schweitzer, S. A., & Cowen, E. A. (2025). Data from: Wind stress effects on drone-based thermal infrared surface velocimetry measurements of tidal flow in an estuary [Dataset]. Cornell University Library eCommons: DeFrees Hydraulics Lab. <https://doi.org/10.7298/p8k3-2p77>
- Holland, K., Holman, R., Lippmann, T., Stanley, J., & Plant, N. (1997). Practical use of video imagery in nearshore oceanographic field studies. *IEEE Journal of Oceanic Engineering*, 22(1), 81–92. <https://doi.org/10.1109/48.557542>
- Hulsing, H. (1967). *Measurement of peak discharge at dams by indirect method*. U.S. Government Printing Office.
- Johnson, E. D., & Cowen, E. A. (2016). Remote monitoring of volumetric discharge employing bathymetry determined from surface turbulence metrics. *Water Resources Research*, 52(3), 2178–2193. <https://doi.org/10.1002/2015WR017736>
- Johnson, E. D., & Cowen, E. A. (2017). Remote determination of the velocity index and mean streamwise velocity profiles. *Water Resources Research*, 53(9), 7521–7535. <https://doi.org/10.1002/2017WR020504>
- Kim, Y., Muste, M., Hauet, A., Krajewski, W. F., Kruger, A., & Bradley, A. (2008). Stream discharge using mobile large-scale particle image velocimetry: A proof of concept. *Water Resources Research*, 44(9), W09502. <https://doi.org/10.1029/2006WR005441>
- Kinzel, P. J., & Legleiter, C. J. (2019). sUAS-based remote sensing of river discharge using thermal particle image velocimetry and bathymetric lidar. *Remote Sensing*, 11(19), 2317. <https://doi.org/10.3390/rs11192317>
- Kinzel, P. J., Legleiter, C. J., & Gazoorian, C. L. (2024). Reach-scale mapping of surface flow velocities from thermal images acquired by an uncrewed aircraft system along the Sacramento River, California, USA. *Water*, 16(13), 1870. <https://doi.org/10.3390/w16131870>
- Koutalakis, P., & Zaimes, G. N. (2022). River flow measurements utilizing UAV-based surface velocimetry and bathymetry coupled with sonar. *Hydrology*, 9(8), 148. <https://doi.org/10.3390/hydrology9080148>
- Laxague, N. J. M., & Zappa, C. J. (2020). Observations of mean and wave orbital flows in the ocean's upper centimetres. *Journal of Fluid Mechanics*, 887, A10. <https://doi.org/10.1017/jfm.2019.1019>
- Lee, E., Yoon, H., Hyun, S. P., Burnett, W. C., Koh, D.-C., Ha, K., et al. (2016). Unmanned aerial vehicles (UAVs)-based thermal infrared (TIR) mapping, a novel approach to assess groundwater discharge into the coastal zone. *Limnology and Oceanography: Methods*, 14(11), 725–735. <https://doi.org/10.1002/lom3.10132>
- Legleiter, C. J., & Kinzel, P. J. (2020). Inferring surface flow velocities in sediment-laden Alaskan rivers from optical image sequences acquired from a helicopter. *Remote Sensing*, 12(8), 1282. <https://doi.org/10.3390/rs12081282>
- Legleiter, C. J., & Kinzel, P. J. (2023). The toolbox for river velocimetry using images from aircraft (TRiVIA). *River Research and Applications*, 39(8), 1457–1468. <https://doi.org/10.1002/rra.4147>
- Legleiter, C. J., Kinzel, P. J., Dille, M., Vespignani, M., Wong, U., Anderson, I., et al. (2024). Mapping river flow from thermal images in approximately real time: Proof of CONCEPT on the Sacramento River, California, USA. *Remote Sensing*, 16(24), 4746. <https://doi.org/10.3390/rs16244746>
- Legleiter, C. J., Kinzel, P. J., Engel, F. L., Harrison, L. R., & Hewitt, G. (2024). A two-dimensional, reach-scale implementation of space-time image velocimetry (STIV) and comparison to particle image velocimetry (PIV). *Earth Surface Processes and Landforms*, 49(10), 3093–3114. <https://doi.org/10.1002/esp.5878>
- Levesque, V. A., & Oberg, K. A. (2012). *Computing discharge using the index velocity method* (Tech. Rep. Nos. 3–A23). U.S. Geological Survey.
- Lewis, Q. W., Lindroth, E. M., & Rhoads, B. L. (2018). Integrating unmanned aerial systems and LSPIV for rapid, cost-effective stream gauging. *Journal of Hydrology*, 560, 230–246. <https://doi.org/10.1016/j.jhydrol.2018.03.008>
- Lin, D., Grundmann, J., & Eltner, A. (2019). Evaluating image tracking approaches for surface velocimetry with thermal tracers. *Water Resources Research*, 55(4), 3122–3136. <https://doi.org/10.1029/2018WR024507>
- Lu, J., Yang, X., & Wang, J. (2023). Velocity vector estimation of two-dimensional flow field based on STIV. *Sensors*, 23(2), 955. <https://doi.org/10.3390/s23020955>
- McAllister, J., Dutrieux, L., fdarvas, Jochym, M., DanielsLouis, rrowlands, et al. (2024). Micasense/imageprocessing [Software]. MicaSense, Inc. Retrieved from <https://github.com/micasense/imageprocessing>
- Muste, M., Hauet, A., Fujita, I., Legout, C., & Ho, H. C. (2014). Capabilities of large-scale particle image velocimetry to characterize shallow free-surface flows. *Advances in Water Resources*, 70, 160–171. <https://doi.org/10.1016/j.advwatres.2014.04.004>
- Muste, M., Schöne, J., & Creutin, J.-D. (2005). Measurement of free-surface flow velocity using controlled surface waves. *Flow Measurement and Instrumentation*, 16(1), 47–55. <https://doi.org/10.1016/j.flowmeasinst.2004.08.003>
- Neumeier, U., & Amos, C. L. (2006). The influence of vegetation on turbulence and flow velocities in European salt-marshes. *Sedimentology*, 53(2), 259–277. <https://doi.org/10.1111/j.1365-3091.2006.00772.x>
- NortekAS. (2017). Aquadopp profiler 1 MHz. Retrieved from <https://www.nortekgroup.com/export/pdf/Aquadopp%20Profiler%201%20MHz.pdf>
- Ortiz-Suslow, D. G., Haus, B. K., Williams, N. J., Laxague, N. J. M., Reniers, A. J. H. M., & Graber, H. C. (2015). The spatial-temporal variability of air-sea momentum fluxes observed at a tidal inlet. *Journal of Geophysical Research: Oceans*, 120(2), 660–676. <https://doi.org/10.1002/2014JC010412>
- Pearce, S., Ljubićić, R., Peña-Haro, S., Perks, M., Tauro, F., Pizarro, A., et al. (2020). An evaluation of image velocimetry techniques under low flow conditions and high seeding densities using unmanned aerial systems. *Remote Sensing*, 12(2), 232. <https://doi.org/10.3390/rs12020232>
- Perks, M. T., Russell, A. J., & Large, A. R. G. (2016). Technical note: Advances in flash flood monitoring using unmanned aerial vehicles (UAVs). *Hydrology and Earth System Sciences*, 20(10), 4005–4015. <https://doi.org/10.5194/hess-20-4005-2016>
- Pinton, D., Canestrelli, A., & Fantuzzi, L. (2020). A UAV-based dye-tracking technique to measure surface velocities over tidal channels and salt marshes. *Journal of Marine Science and Engineering*, 8(5), 364. <https://doi.org/10.3390/jmse8050364>
- Pirelli, L. (2019). Camera\_calculator.py [Software]. Retrieved from <https://gist.github.com/luipir/dc33864b53cf6634f9cdd2bce712d3d9>
- Pizarro, A., Dal Sasso, S. F., & Manfreda, S. (2022). VISION: VVideo StabilisatION using automatic features selection for image velocimetry analysis in rivers. *SoftwareX*, 19, 101173. <https://doi.org/10.1016/j.softx.2022.101173>

- Puleo, J. A., McKenna, T. E., Holland, K. T., & Calantoni, J. (2012). Quantifying riverine surface currents from time sequences of thermal infrared imagery. *Water Resources Research*, 48(1), W01527. <https://doi.org/10.1029/2011WR010770>
- Rantz, S. E. (1982). *Measurement and computation of streamflow*. U.S. Department of the Interior, Geological Survey.
- Schweitzer, S. A., & Cowen, E. A. (2021). Instantaneous river-wide water surface velocity field measurements at centimeter scales using infrared quantitative image velocimetry. *Water Resources Research*, 57(8), e2020WR029279. <https://doi.org/10.1029/2020WR029279>
- Schweitzer, S. A., & Cowen, E. A. (2022). A method for analysis of spatial uncertainty in image based surface velocimetry. *Frontiers in Water*, 4, 744278. <https://doi.org/10.3389/frwa.2022.744278>
- Schwendeman, M., & Thomson, J. (2015). Observations of whitecap coverage and the relation to wind stress, wave slope, and turbulent dissipation. *Journal of Geophysical Research: Oceans*, 120(12), 8346–8363. <https://doi.org/10.1002/2015JC011196>
- Silva, G. D., Roberts, D. A., McFadden, J. P., & King, J. Y. (2022). Shifts in salt marsh vegetation landcover after debris flow deposition. *Remote Sensing*, 14(12), 2819. <https://doi.org/10.3390/rs14122819>
- Sutherland, P., & Melville, W. K. (2015). Field measurements of surface and near-surface turbulence in the presence of breaking waves. *Journal of Physical Oceanography*, 45(4), 943–965. <https://doi.org/10.1175/JPO-D-14-0133.1>
- Tauro, F., Pagano, C., Phamduy, P., Grimaldi, S., & Porfiri, M. (2015). Large-scale particle image velocimetry from an unmanned aerial vehicle. *IEEE/ASME Transactions on Mechatronics*, 20(6), 3269–3275. <https://doi.org/10.1109/TMECH.2015.2408112>
- Thumser, P., Haas, C., Tuhtan, J. A., Fuentes-Pérez, J. F., & Toming, G. (2017). RAPTOR-UAV: Real-time particle tracking in rivers using an unmanned aerial vehicle. *Earth Surface Processes and Landforms*, 42(14), 2439–2446. <https://doi.org/10.1002/esp.4199>
- Tomasi, C., & Kanade, T. (1992). Shape and motion from image streams under orthography: A factorization method. *International Journal of Computer Vision*, 9(2), 137–154. <https://doi.org/10.1007/BF00129684>
- Torres-Rua, A. (2017). Vicarious calibration of sUAS microbolometer temperature imagery for estimation of radiometric land surface temperature. *Sensors*, 17(7), 1499. <https://doi.org/10.3390/s17071499>
- UCNRS. (2022). Carpinteria [Dataset]. <https://doi.org/10.21973/N3X08Q>
- UCNRS. (2023). Carpinteria salt marsh reserve archives—Natural reserve system. Retrieved from <https://ucnrs.org/reserves/carpinteria-salt-marsh-reserve/>
- USGS. (2022). Carpinteria C NR Carpinteria CA [Dataset]. Retrieved from <https://waterdata.usgs.gov/monitoring-location/11119500/>
- Veron, F., & Melville, W. K. (2001). Experiments on the stability and transition of wind-driven water surfaces. *Journal of Fluid Mechanics*, 446, 25–65. <https://doi.org/10.1017/S0022112001005638>
- Voulgaris, G., & Meyers, S. T. (2004). Temporal variability of hydrodynamics, sediment concentration and sediment settling velocity in a tidal creek. *Continental Shelf Research*, 24(15), 1659–1683. <https://doi.org/10.1016/j.csr.2004.05.006>
- Wüest, A., & Lorke, A. (2003). Small-scale hydrodynamics in lakes. *Annual Review of Fluid Mechanics*, 35(1), 373–412. <https://doi.org/10.1146/annurev.fluid.35.101101.161220>
- Young, D. L., Bruder, B. L., Haas, K. A., & Webster, D. R. (2016). The hydrodynamics of surface tidal flow exchange in saltmarshes. *Estuarine, Coastal and Shelf Science*, 172, 128–137. <https://doi.org/10.1016/j.ecss.2016.02.006>
- Zappa, C. J., Raymond, P. A., Terray, E. A., & McGillis, W. R. (2003). Variation in surface turbulence and the gas transfer velocity over a tidal cycle in a macro-tidal estuary. *Estuaries*, 26(6), 1401–1415. <https://doi.org/10.1007/BF02803649>

## Erratum

The originally published version of this article contained a typographical error in Tables 2 and 3, where the values were inadvertently swapped. The error has been corrected, and this may be considered the authoritative version of record.